Progress in Reaction Kinetics and Mechanism

ARTICLE

Open Access

https://doi.org/10.48130/prkm-0026-0019

Progress in Reaction Kinetics and Mechanism **2026**, 51: e025

A long-neglected reaction in pyrolysis and combustion

Shiling Wei[1], Bingzhi Liu[2], Zhongxin Tang[1], Jinyu Tan[1], Zhandong Wang[2*] and Lixia Wei[1*]

[1] *School of Mechanical Engineering, Guangxi University, Nanning, Guangxi 530004, China*

[2] *National Synchrotron Radiation Laboratory, University of Science and Technology of China, Hefei, Anhui 230029, China*

* Correspondence: zhdwang@ustc.edu.cn (Wang Z); feilix@gxu.edu.cn (Wei L)

Abstract

Backside attack reactions, a type of bimolecular nucleophilic substitution, in solutions have attracted increasing attention from researchers. However, similar reactions in the gas phase, especially in pyrolysis and combustion, have been scarcely reported. In this work, several bimolecular nucleophilic substitution-style reactions of ethylene oxide (EO) and methanol (CH_3OH) are proposed and incorporated into the AramcoMech 3.0 mechanism. By comparing the experimental data from this study with values reported in the literature, the influence of these reactions on prediction of the combustion mechanism was verified. The newly added reactions substantially improve the prediction for formaldehyde, one of the major species in EO pyrolysis. However, the overall contribution of the backside attack reactions to EO pyrolysis is less. The laminar burning velocities (LBVs) of EO are predicted to decrease slightly when the newly proposed reactions are included in the AramcoMech 3.0 mechanism. At the same time, the backside attack reactions resulted in a minor improvement in the prediction of CH_3OH's LBV under rich combustion conditions. Generally speaking, the newly proposed backside attack reactions play a non-negligible role in the gas phase.

Keywords: Backside attack, Ethylene oxide, Laminar burning velocity, Pyrolysis, S_N2

Citation: Wei S, Liu B, Tang Z, Tan J, Wang Z, et al. 2026. A long-neglected reaction in pyrolysis and combustion. *Progress in Reaction Kinetics and Mechanism* 51: e025 https://doi.org/10.48130/prkm-0026-0019

Introduction

In 1937, Cowdrey et al.[1] proposed the reaction mechanism for nucleophilic substitution. A nucleophilic substitution reaction occurs when a nucleophile bearing a negative or partial negative charge attacks a carbon atom carrying a positive or partial positive charge, thereby causing the displacement of a group attached to the carbon atom. Bimolecular nucleophilic substitution (S_N2), as a typical nucleophilic substitution reaction, includes two pathways, i.e., backside attack and frontside attack. Over the past few decades, S_N2 has attracted widespread attention from experimentalists and theorists. Han et al.[2] reported the Atherton–Todd reaction of pentacoordinate hydrospirophosphorane with phenolic compounds, which proceeds via a halogenated spirophosphorane intermediate with retention of phosphorus configuration, followed by nucleophilic substitution at the P-V atom of halogenated spirophosphorane. Backside attack is the dominant pathway for nucleophilic substitution of the P–Cl bond. Liang et al.[3] developed a mild and efficient nucleophilic halogen substitution (S_N2X) to achieve sulfinylation of activated tertiary alkyl halides. The reaction follows an S_N2X pathway via frontside attack at the halogen and is insensitive to steric hindrance on the backside. Sekiguchi et al.[4] proposed a novel S_NV alkenyl substitution of 1-fluoro-1-alkenylmagnesium chloride with Grignard reagents through C–F bond cleavage. Mechanistic investigations reveal that the magnesium center activates the C–F bond to facilitate the S_NV pathway. Tsujibayashi et al.[5] explored the trifluoromethylation mechanism using Umemoto's reagent via *ab initio* and DFT calculations, confirming an ionic backside mechanism for this transformation. Satpathy et al.[6] investigated the effects of solvent polarity on the potential energy surface (PES) of the S_N2 reaction F^- + CH_3Cl and found that increase in solvent polarity markedly increases the reaction energy barrier. Domingo et al.[7] adopted the molecular electron density theory to investigate the S_N2 and S_Ni reactions of monosubstituted methyl compounds in DMSO via ωB97X-D/6-311 + G(*d*,*p*) calculations. In their work, they revised the traditional hypervalent-carbon transition-state viewpoint and clarified the intrinsic electronic features governing these substitution pathways. However, all these investigations focused on solutions. This work reports similar reactions in pyrolysis and combustion, including the investigation of S_N2-style reactions in the gas phase and its effect on the performance of the related combustion mechanisms, by considering ethylene oxide (EO) and methanol (CH_3OH) as the models.

Thirteen backside attack reactions closely associated with EO and CH_3OH are proposed, with their rate parameters calculated at the CCSD(T)/cc-pVQZ levels. Through validation of the mole fractions of EO pyrolysis intermediates and the laminar burning velocities (LBVs) of EO and CH_3OH, the effects of these reactions on the performance of relevant combustion mechanisms were confirmed. In the experimental part, a jet-stirred reactor (JSR) was used to conduct EO pyrolysis at a temperature of 750–1080 K and a pressure of 760 Torr. The experimental data related to LBV of CH_3OH are reported in Wang et al.[8]. LBVs of EO are simulated with and without the newly conceived reactions in this work.

Experimental methods

The EO pyrolysis experiments were completed at the National Synchrotron Radiation Laboratory in the University of Science and Technology of China. Detailed information regarding this experimental apparatus has been comprehensively documented and discussed in the literature[9,10]. This paper provides only a brief introduction. The experimental platform mainly consists of five parts, i.e., a computer-controlled sample syringe pump system, a JSR, a tubular heating furnace, an ultrasonic molecular beam sampling system, and a reflection time-of-flight mass spectrometer. Figure 1 shows a schematic sketch of the devices used for EO pyrolysis experiments at 760 Torr.

https://doi.org/10.48130/prkm-0026-0019

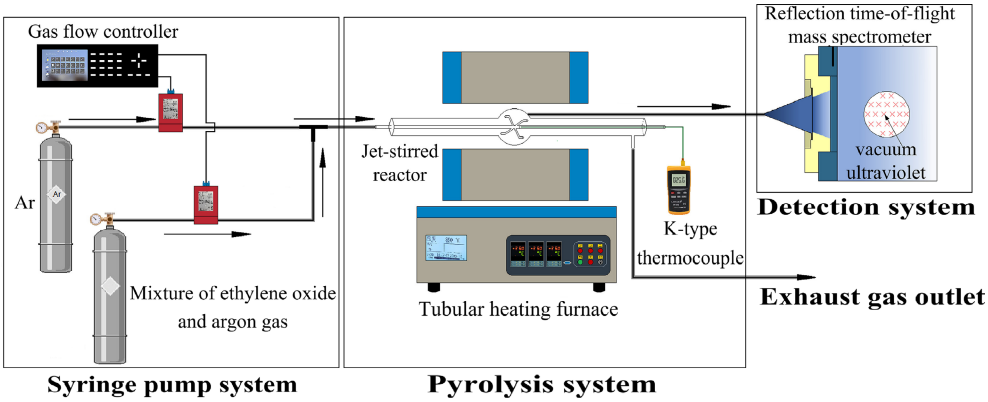

Fig. 1 Schematic sketch of the experimental apparatus for ethylene oxide pyrolysis.

The mixture of EO and argon (Ar), purchased from Nanjing Special Gas Factory Co., Ltd. in China, and high-purity Ar (99.999% purity) were introduced into the JSR with a volume of 78 cm^3. The proportion of EO used was 0.5% by mole fraction. The gas flow rate was accurately adjusted through the MKS flow controller to ensure that the residence time of the reactants in the reactor was 2 s. The reaction temperature was monitored in real time by a K-type thermocouple, whose measurement error does not exceed 10 K. The pyrolysis products produced of EO were collected by an ultrasonic molecular beam sampling device, ionized by vacuum ultraviolet synchrotron radiation, and finally detected and measured by a reflection time-of-flight mass spectrometer.

The experiments were conducted at 760 Torr and the temperature range was controlled between 750 and 1,080 K. The pyrolysis products at three different photon energies (i.e., 10.5, 11.5, and 14.5 eV) were measured in the experiment. The identification and measurement methods for relevant species have been well described in previous studies[11]. The photoionization cross-section (PICS) data of EO can be found in the article published by Fófano et al.[12]. The relevant data for other pyrolysis products can be found in the online database provided in ref. [13]. For those species whose PICS is known, the experimentally measured mole fraction error is approximately 25%; for those species whose PICS can only be estimated, the uncertainty of the experimental mole fraction is within a factor of 2[11].

Theoretical methods and kinetic model

Rate constant calculations

Gaussian16 software[14] and the Master Equation System Solver (MESS) computer code were used to calculate the rate constants and energies of the backside attack reactions.

Firstly, at the calculation level of B3LYP/6-311 + G(*d*,*p*)[15–17], the PESs of the backside attack reactions were scanned to obtain the vibrational frequencies, zero-point energies (ZPEs), and hindrance potentials of the reactants and products, and the transition states of the optimized geometries. In order to confirm that the obtained transition state indeed correctly connects the specified reactants and products, intrinsic reaction coordinate (IRC) calculations were also performed[18]. The single-point energies of the species were calculated at the higher-precision CCSD(T)/cc-pVQZ level[19,20].

Secondly, the rate constants of these reactions were calculated in the temperature range from 720 to 1080 K and at pressures of 0.01, 0.1, 1, 10, and 100 atm. The calculations were based on transition state theory[21,22] and were done by solving the master equation. The molecular coordinates, vibrational frequencies, energies, and hinderance potentials calculated using Gaussian16 software were considered as the MESS input data to calculate the rate constants. In this process, a one-dimensional single exponential down model was used, $\langle\Delta E_{down}\rangle = 180*(T/298)^{0.95}$ cm^{-1}[23], to approximately represent the probability of collision energy transfer. The collision frequency between the reactants and bath gases was estimated using the Lennard–Jones (L–J) model. The L–J parameter values for EO and the bath gas, Ar, were taken from Wang et al.[23], as per which their σ values are 5.84 and 3.47 Å, respectively, and ε values are 248.96 and 78.89 cm^{-1}, respectively. The L–J parameters of the products formed in the backside attack reactions were obtained from the Reaction Mechanism Generator (RMG) molecular database[24]. The detailed L–J parameter values of these substances can be found in Supplementary Table S1 of Supplementary materials. For small molecules with available accurate experimental measurements, the database adopts L–J parameters derived directly from experimental fitting. For macromolecules and intermediate radicals lacking experimental transport data, the database first estimates critical physical properties, including critical temperature, critical pressure, and critical volume, using the Joback group additivity method. The corresponding L–J parameters are then converted via the classical physical-property correlation equations, which constitute a reliable semi-empirical estimation approach. In this work, the L–J parameters of all products from the backside attack reactions were determined using this semi-empirical estimation method.

The detailed reactions proposed in this work and the corresponding kinetic parameters are shown in Supplementary Table S2.

Kinetic modeling

The AramcoMech 3.0 mechanism[25] was updated by incorporating the 5 newly conceived species and the 13 newly proposed reactions, resulting in a detailed kinetic model comprising 586 species and 3,049 reactions. The kinetic, thermodynamic, and transport parameters of the original mechanism remain unchanged. The thermodynamic and transport parameters of the newly added species were obtained from the RMG molecular database[25]. This database provides the thermodynamic parameters of these species, taken from the "DFT_QCI_thermo" library, which contains thermochemical parameters calculated by high-precision quantum chemical methods based on DFT/QCI, including the standard enthalpy of formation, standard entropy, and temperature-dependent heat capacities. The transport parameters of the newly added species were obtained using the group additivity estimation method. The

structures and names of the main species can be found in Supplementary Table S3 in Supplemental materials.

The pyrolysis simulation of EO was performed using the perfectly stirred reactor (PSR) module in the Chemkin-Pro software. All PSR simulations of EO pyrolysis were conducted under isothermal conditions. The reactor temperature was fixed at discrete values in the range of 750–1,080 K. The LBVs of EO and CH_3OH were calculated using the Premixed Laminar Flame Speed Calculation module. The computational domain length for the simulation was set to 5.0 cm, with an axial starting position of 0.0 cm. The grid system was configured with a maximum of 500 grid points, including 10 adaptive grid points. To accurately capture the temperature and species gradient variations in the flame front region, the adaptive grid control thresholds for both the solution gradient and curvature were set to 0.01. The oxidizer used was air.

Results and discussion

Effects of backside attack reactions on EO pyrolysis

Backside attack reactions on EO

Due to the symmetry of the EO molecule, backside attack reactions may occur at three positions, i.e., (a) on the carbon atom from the side opposite the oxygen atom; (b) on the carbon atom from the side opposite the other carbon atom; and (c) on the oxygen atom from the side opposite a carbon atom, as shown in Fig. 2. Figure 3 shows the energy profiles of these backside attack reactions, along with their rate constants at T = 750–1,080 K and 1 atm.

The first case involves a backside attack by the H atom on the EO on C(2) from the side opposite the oxygen atom to form the C(2)–H bond (direction a in Fig. 2), while the C(2)–O(1) bond cleaves, resulting in the formation of the ethoxyl radical (C_2H_5O). The energy barrier for this reaction, EO + H = C_2H_5O (R1), is 12.49 kcal·mol^{-1}, as shown in Fig. 3. The second case involves a backside attack by the H atom on the EO on C(2) from the side opposite C(3) to form the C(2)–H bond (direction b), while the C(2)–C(3) bond cleaves, resulting in the formation of methoxymethyl (CH_3OCH_2). The energy barrier for this reaction, EO + H = CH_3OCH_2 (R2), is 20.99 kcal·mol^{-1}. The third case involves a backside attack by the H atom on the EO on O(1) from the side opposite C(2) to form the O(1)–H bond (direction c), while the O(1)-C(2) bond cleaves, resulting in the formation of 2-hydroxylethyl (PC_2H_4OH). The energy barrier for this reaction, EO + H = PC_2H_4OH (R3), is 16.41 kcal·mol^{-1}.

Among the three reactions, R1 has the highest rate constant, followed by R3, while R2 has the lowest rate constant, about ten times lower than R1 and R3, as shown in Fig. 3b. This trend follows that of the reaction energy barriers of the three reactions. The lengths of the C–O and C–C bonds of EO are calculated to be 143 and 146 pm in this work. In comparison with the typical bond lengths of C–O and C–C in ethanol (C_2H_5OH)[26], i.e., 143 and 154 pm, respectively, the C–C bond in EO is shortened obviously. This indicates that the C–C bond strength is strengthened in EO. Consequently, this strengthened bond results in higher energy barriers and hence lower reaction rate constants for backside attacks that cleave the C–C bond. This makes the cleavage of the C–O bond in EO pyrolysis a more competitive pathway.

The backside attack reactions by OH and CH_3 on EO, as well as similar reactions on CH_3OH, were also investigated in this work, as shown in Supplementary Figs. S1–S3 of Supplementary materials. It is clear that the rate constants of the backside attack reactions by the H atom are higher than those by OH and CH_3. Since the steric hindrance follows the trend CH_3 > OH > H atom, the highest rate constants for the backside attack reactions by the H atom are expected.

Effect of backside attack reactions on EO pyrolysis

Figures 4 and 5 compare the performance of the AramcoMech 3.0 mechanism and the updated mechanism against the experimental results of EO pyrolysis. It can be seen from the figures that, except for formaldehyde (CH_2O), adding the 13 backside attack reactions has little effect on the mole fraction of the main pyrolysis products of EO. This is particularly evident in Fig. 5, where the updated mechanism is shown to greatly improve the prediction results for CH_2O.

To further demonstrate this difference, the flow rate of CH_2O was analyzed at 900 K, corresponding to 79.2% consumption of EO, as shown in Fig. 6.

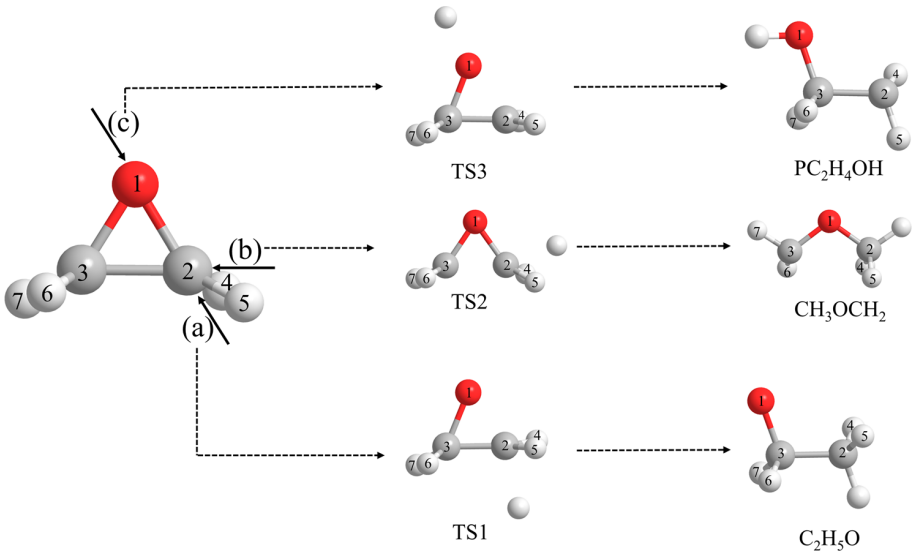

Fig. 2 The transition states and products formed in the backside attack reaction by the H atom on EO from three directions: (a) on the carbon atom from the side opposite the oxygen atom; (b) on the carbon atom from the side opposite the other carbon atom; (c) on the oxygen atom from the side opposite the carbon atom.

https://doi.org/10.48130/prkm-0026-0019

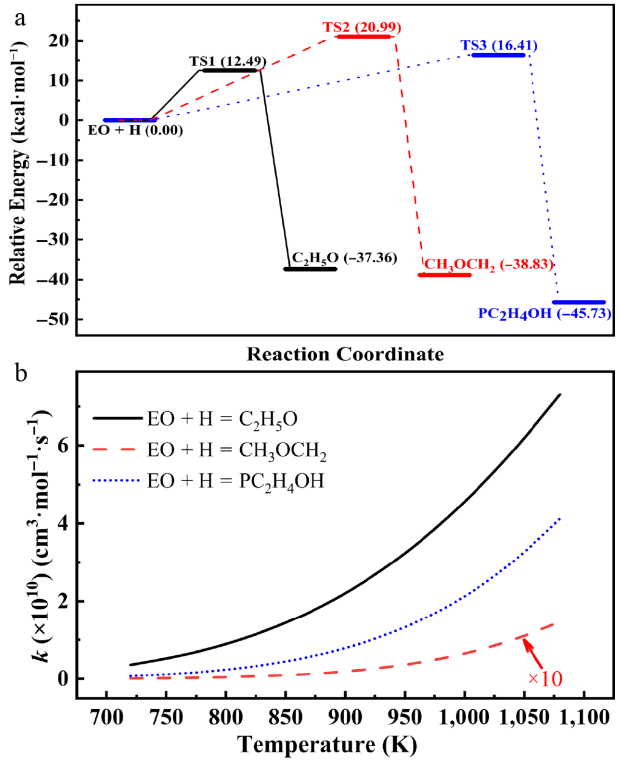

Fig. 3 Potential energy profiles (a) of the backside attack reactions by the H atom on EO, and the corresponding rate constants at 750–1,080 K and 1 atm (b).

It can be seen that the main consumption pathways of EO include the ring-opening isomerization to CH_3CHO, H-abstraction reactions, and decomposition to CH_3 + HCO, consistent with the conventional mechanism. The backside attack reactions by H atom on EO (R1 and R3) account for 1.2% of the EO consumption. Since these newly added backside attack reactions contribute marginally to the consumption of EO, the contributions of the isomerization and decomposition reactions remain almost unchanged, while that of the hydrogen abstraction reaction in which the hydrogen atom participates, EO + H = C_2H_3O1-2 + H_2 (R14), decreases from 20.8% to 19.6%. Since the backside attack reactions by the H atom, R1 and R3, compete with this H-abstraction reaction, the contribution of R1 and R3 to EO consumption is at the cost of the decreased contribution of this H-abstraction reaction by the H atom.

Since the contributions of R1 and R3 are negligible, the mole fraction distribution curves of most substances during the pyrolysis of EO should remain essentially unchanged, as shown in Fig. 4. However, consumption of C_2H_5O, the only product of R1, overwhelmingly leads to the production of CH_2O via the decomposition pathway $C_2H_5O \rightarrow CH_3 + CH_2O$, contributing to 99.8% of both C_2H_5O consumption and CH_2O production. Therefore, as shown in Fig. 5, the current mechanism can greatly improve the production of CH_2O. Thus, it can be inferred that the backside attack reactions do occur in the gas phase.

As for R3, its effect on EO consumption is negligible. Theoretically, R3 can promote the formation of C_2H_4; however, this increase is insignificant due to the minor contribution of R3 and the already high mole fraction of C_2H_4, as shown in Fig. 4.

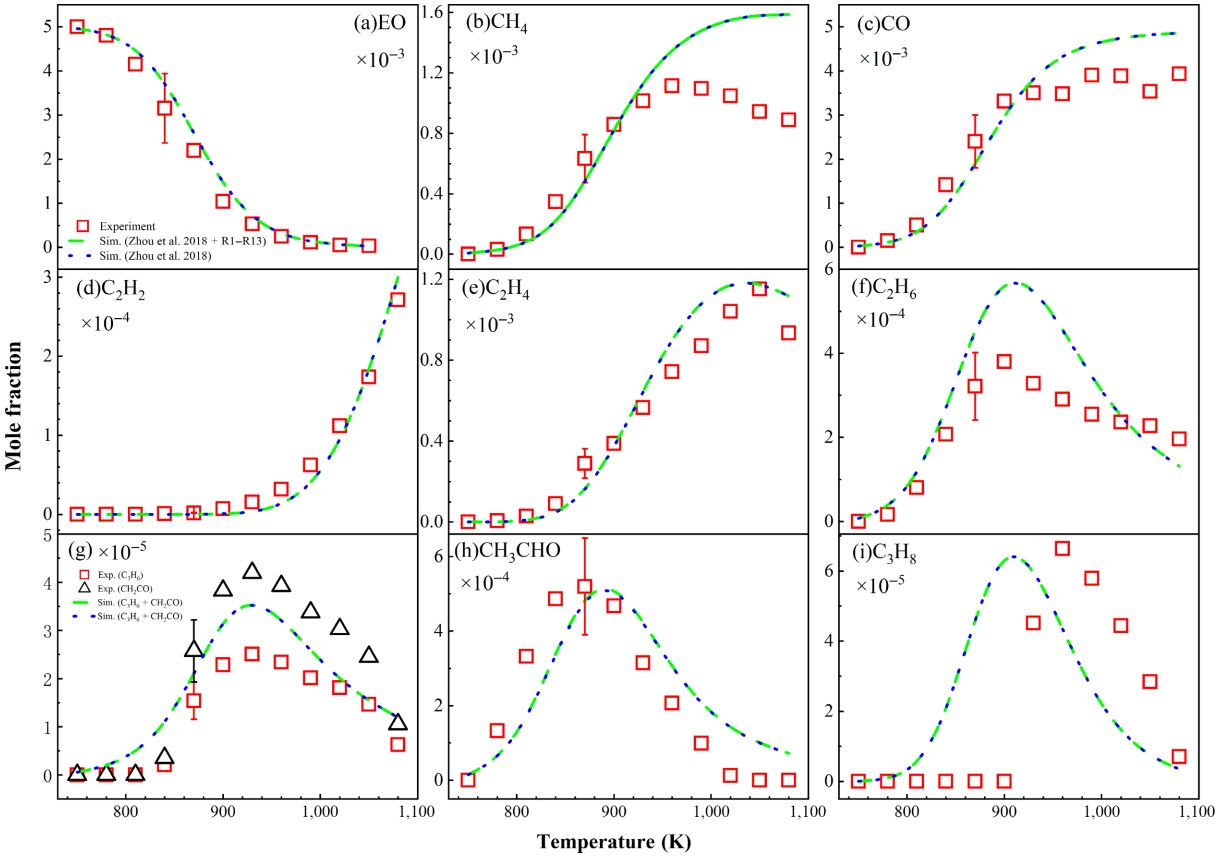

Fig. 4 Experimental mole fraction (symbol representation) and simulated mole fraction (line representation) curves of ethylene oxide pyrolysis products: (a) ethylene oxide (EO), (b) methane (CH_4), (c) carbon monoxide (CO), (d) acetylene (C_2H_2), (e) ethylene (C_2H_4), and (f) ethane (C_2H_6). (g) Experimental mole fraction distributions for propylene (C_3H_6) and ketene (CH_2CO), and simulated mole fraction curves for the reaction between C_3H_6 and CH_2CO, (h) acetaldehyde (CH_3CHO), and (i) propane (C_3H_8).

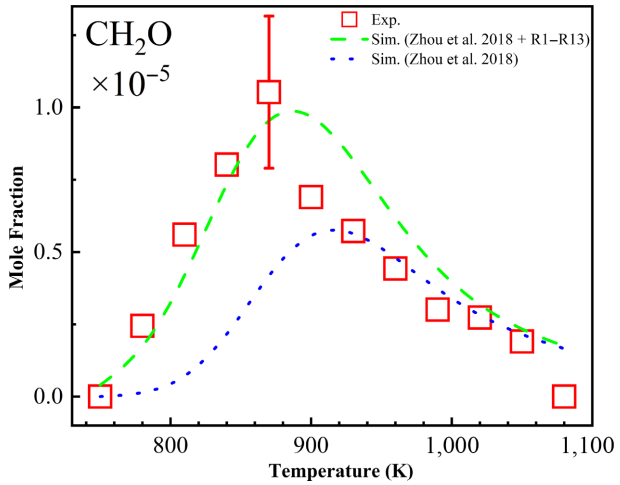

Fig. 5 Experimental mole fraction (symbol representation) and simulated mole fraction (line representation) of CH_2O, a product of ethylene oxide pyrolysis.

Thus, generally speaking, the backside attack reactions contribute marginally to the pyrolysis of EO.

Effect of backside attack reactions on the laminar burning velocities of EO

In order to further explore the impact of the backside attack reactions on the combustion performance of EO, LBVs were also simulated using EO–air mixtures at 358, 473, and 500 K at 1 atm, as well as at 1, 4, and 8 atm at 500 K, as shown in Fig. 7.

Figure 7 demonstrates that incorporation of the backside attack reactions reduces the LBV of EO at different temperatures and pressures. At 1 atm, the simulated peak LBV values for EO are 103.7, 177.2, 202.1 cm s^{-1} and 104.1, 177.6, 203.7 cm s^{-1}, by the AramcoMech 3.0 mechanism, with and without the backside attack reactions at 358, 473, and 500 K, respectively. Incorporation of the backside attack reactions reduces the peak LBV values of EO by 0.4, 0.4, and 1.6 cm s^{-1}, corresponding to a reduction of 0.4%, 0.2%, and 0.8%, respectively. Meanwhile, at 500 K, the simulated peak LBV values for EO are 202.1, 141.7, 131.1 cm s^{-1} and 203.7, 143.9, 133.5 cm s^{-1}, by the AramcoMech 3.0 mechanism, with and without the backside attack reactions, at 1, 4, 8 atm, respectively. Incorporation of the backside attack reactions reduces the peak LBV values of EO by 1.6, 2.2, and 2.4 cm s^{-1}, corresponding to a reduction of 0.8%, 1.5%, and 1.8%, respectively. This pressure-dependent behavior originates from the AramcoMech 3.0 mechanism.

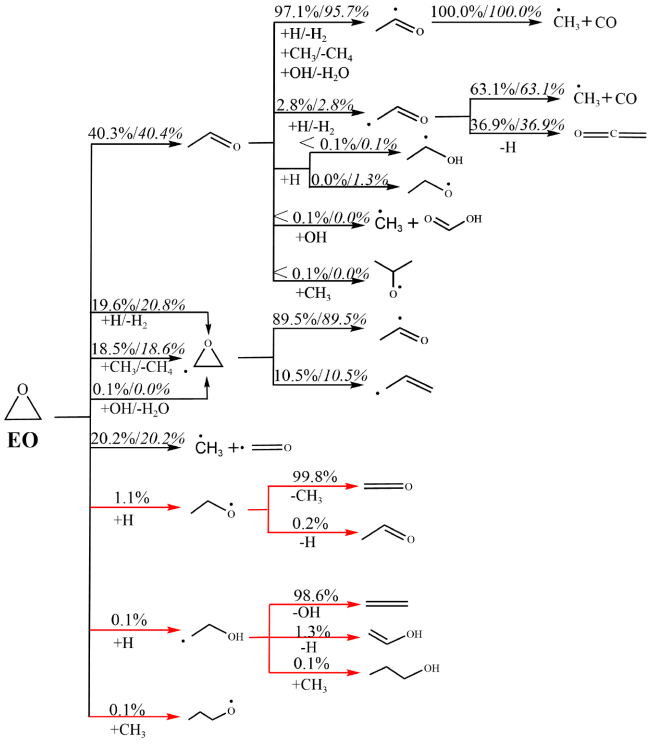

Fig. 6 Flow-rate analysis of ethylene oxide pyrolysis at 900 K. Percentages in normal font are related to the updated mechanism, while those in italics are related to the AramcoMech 3.0 mechanism.

To reveal the mechanism responsible for the lower predicted LBV of EO, sensitivity analysis of LBV was compared using both the original and updated mechanisms at 500 K and 1 atm, as shown in Supplementary Fig. S4. It can be seen that the dominant chain-branching reaction, $O_2 + H = O + OH$, is the most sensitive one in increasing the LBV of EO. After incorporating reactions R1–R13, its sensitivity coefficient decreases noticeably, which is natural since

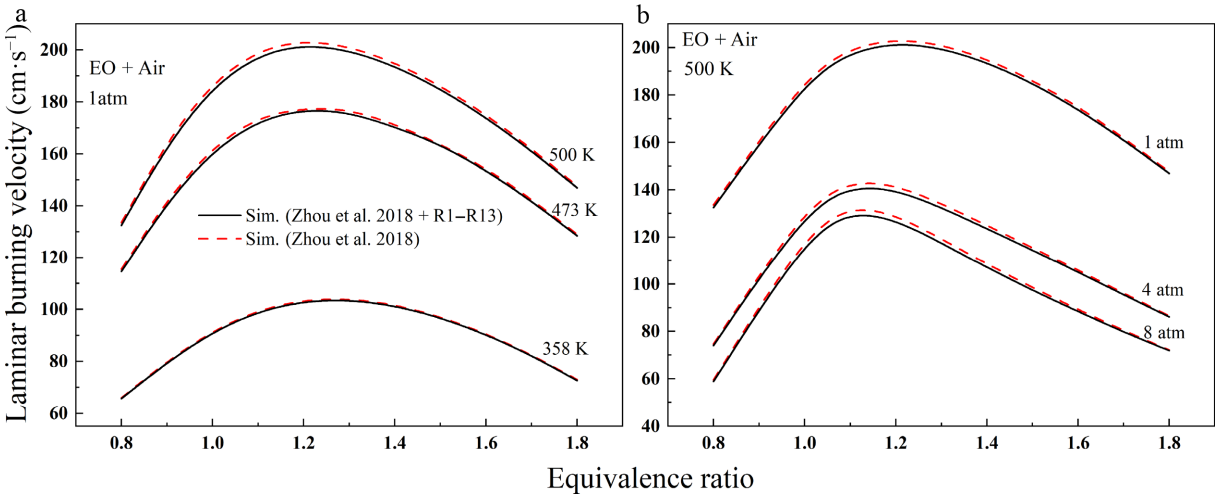

Fig. 7 The laminar burning velocity of EO (a) at 358, 473, and 500 K at 1 atm, and (b) at 1, 4, and 8 atm at 500 K.

https://doi.org/10.48130/prkm-0026-0019

the newly proposed backside attack reactions, R1, R2, and R3, competitively consume the H atoms and lower the LBV. Meanwhile, the backside attack reaction, $C_2H_4O1\text{-}2 = CH_3 + HCO$, simultaneously increases the LBV. As a result, the backside attack reactions ultimately lower the LBV of EO only slightly.

Sensitivity analysis of LBV for EO at different temperatures and pressures with an equivalent ratio of 1.2, as shown in Supplementary Figs. S5 and S6, indicates that the backside attack reaction by the H atom on EO, R3, is the most sensitive reaction among the proposed backside attack reactions. However, its sensitivity only ranks 9–14 in reducing the LBV of EO. This result is expected since these H-consuming reactions contribute marginally to the consumption of EO in pyrolysis.

Effects of backside attack reactions on laminar burning velocities of CH_3OH

The backside attacks on CH_3OH include three reactions: $CH_3OH + H = CH_4 + OH$ (R11), $CH_3OH + H = CH_3 + H_2O$ (R12), and $CH_3OH + OH = CH_3 + H_2O_2$ (R13). R11 involves the backside attack by the H atom on the C atom of CH_3OH to form a C–H bond, while the C–O bond cleaves, leading to CH_4 and OH generation. R12 involves the backside attack by the H atom on the O atom of CH_3OH to form an O–H bond, while the C–O bond cleaves, leading to CH_3 and H_2O generation. R13 involves the backside attack by OH on the O atom of CH_3OH to form the O–O bond, while the C–O bond cleaves, leading to CH_3 and H_2O_2 generation. The effect of these backside attack reactions on the LBV of CH_3OH is demonstrated in Fig. 8, by comparison with the experimental data for CH_3OH. The entire work is based on the experimental condition of CH_3OH–air mixtures under standard thermodynamic conditions.

Figure 8 shows that, basically, incorporation of the backside attack reactions has no effect on the simulated LBV of CH_3OH at the lean side, whereas it reduces the simulated LBV of CH_3OH under fuel-rich conditions. As the equivalence ratio increases, the predicted LBV is further reduced to the experimental values under fuel-rich conditions. The simulated peak LBV values for CH_3OH are 45.3 and 45.5 cm s^{-1}, respectively, around the equivalence ratio of 1.2, by the AramcoMech 3.0 mechanism, with and without the backside attack reactions. At the equivalence ratio of 1.4, the simulated LBV values are 41.6 and 42.1 cm s^{-1}, respectively, by the AramcoMech 3.0 mechanism, with and without the backside attack reactions. Incorporation of the backside attack reactions improves the prediction of the LBV of CH_3OH, since the original mechanism overestimates the LBV at the rich side. Although the improvement in our experiments is minor, adding the backside attack reactions is undoubtedly the right direction to reverse this overestimation. The changes in LBV are outside of the experimental uncertainty, obviously at the rich side in the case of CH_3OH, as shown in Fig. 8.

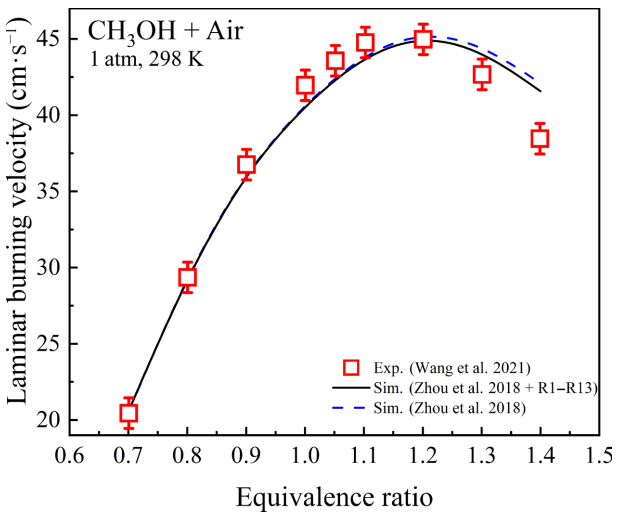

Fig. 8 Comparison of experimental (symbol representation)[8] and simulated (line representation)[25] curves of LBV of CH_3OH at 1 atm and 298 K.

To further demonstrate this difference, the sensitivity analysis of the LBV of CH_3OH was conducted at the equivalent ratio of 1.4, as shown in Supplementary Fig. S7, which indicated that the backside attack reaction by the H atom on CH_3OH, R12, is the most sensitive reaction among the proposed backside attack reactions. However, its sensitivity only ranks 29 in reducing the LBV of CH_3OH. Although the newly added backside attack reactions ranked relatively low, they still improved the predictive performance of AramcoMech 3.0. Adding more backside attack reactions related to CH_3OH may further enhance the predictive performance of the AramcoMech 3.0 mechanism for the LBV of CH_3OH.

Conclusions

In this work, backside attack reactions were conceived and incorporated into the current C0–C4 combustion mechanism. The effects of these reactions on the performance of the AramcoMech 3.0 mechanism were investigated, taking EO and CH_3OH as the examples. The rate constants for these backside attack reactions were calculated using Gaussian16 software and the MESS computer code. EO pyrolysis experiments were performed in a JSR using synchrotron radiation vacuum ultraviolet photoionization mass spectrometry in the temperature range of 750–1,080 K and at a pressure of 760 Torr. The experimental LBV of CH_3OH is from the reported work. Simulated LBVs of EO were calculated using the Chemkin-Pro software with and without the newly conceived reactions in this work.

Incorporating the backside attack reactions remarkably improved the predicted mole fraction of formaldehyde in the pyrolysis of EO, due to the consumption of C_2H_5O, which is produced from the backside attack on EO by the hydrogen atom targeting a carbon atom from the side opposite the oxygen atom. Incorporating the backside attack reactions may also reduce the simulated laminar burning velocity of EO at different temperatures and pressures. For CH_3OH, incorporating the backside attack reactions may improve the prediction accuracy of its LBV at the rich side.

This work demonstrates that backside attack reactions play a non-negligible role in the gas phase, although the improvement in prediction is not so significant. The method proposed in this study is undoubtedly the right direction toward further improving the performance of the current models.

Author contributions

The authors confirm their contributions to this study as follows: writing of the original draft: Wei S; investigation: Wei S, Tang Z; validation: Wei S; software: Wei S, Liu B; data curation: Liu B; visualization: Tan J; methodology: Wang Z; resources: Wang Z, Wei L; conceptualization: Wei L; writing, reviewing, and editing: Wei L; funding acquisition: Wei L. All authors reviewed the results and approved the final version of the manuscript.

Data availability

All data generated or analyzed during this study are included in this published article and its supplementary information files.

Acknowledgments

This work was supported by the project sponsored by the National Natural Science Foundation of China (Nos. 52176102 and 51776045).

Conflict of interest

The authors declare no competing financial interests or personal relationships that could have appeared to influence the work reported in this paper.

Supplementary information accompanies this paper online at: https://doi.org/10.48130/prkm-0026-0019.

Dates

Received 7 May 2026; Revised 12 June 2026; Accepted 13 July 2026; Published online 2 September 2026

References

[1] Cowdrey WA, Hughes ED, Ingold CK, Masterman S, Scott AD. 1937. 257. Reaction kinetics and the walden inversion. Part VI. Relation of steric orientation to mechanism in substitutions involving halogen atoms and simple or substituted hydroxyl groups. *Journal of the Chemical Society* 140:1252−1271

[2] Han K, Wang Y, Zhao P, You X, Wang J, et al. 2021. Investigation of the stereochemical mechanism of the nucleophilic substitution reaction at pentacoordinate phosphorus of spirophosphorane. *The Journal of Organic Chemistry* 86(6):4512−4531

[3] Liang KC, Ling TP, Qin HT, Liu F. 2025. Sulfinylation of tertiary alkyl halides via a halogenophilic substitution (S_N2X) reaction. *The Journal of Organic Chemistry* 90(16):5393−5397

[4] Sekiguchi K, Kimura T. 2025. Nucleophilic vinylic substitution of 1-fluoroalk-1-enylmagnesium chlorides with Grignard reagents *via* C–F bond cleavage. *Tetrahedron* 173:134459

[5] Tsujibayashi S, Kataoka Y, Hirano S, Matsubara H. 2018. An *ab initio* and DFT study of trifluoromethylation using Umemoto's reagent. *Organic and Biomolecular Chemistry* 16(24):4517−4526

[6] Satpathy L, Sahoo S, Sahu PK, Behera PK, Mishra BK. 2018. Effect of solvent polarity on the potential energy surface in the S_N2 reaction of $F^- + CH_3Cl$. *Computational and Theoretical Chemistry* 1150:18−25

[7] Domingo LR, Pérez P, Ríos-Gutiérrez M, Aurell MJ. 2024. A molecular electron density theory study of the bimolecular nucleophilic substitution reactions on monosubstituted methyl compounds. *Organic and Biomolecular Chemistry* 22(36):7425−7437

[8] Wang Z, Han X, He Y, Zhu R, Zhu Y, et al. 2021. Experimental and kinetic study on the laminar burning velocities of NH_3 mixing with CH_3OH and C_2H_5OH in premixed flames. *Combustion and Flame* 229:111392

[9] Chen J, Jiang S, Yang P, Wang L. 2025. Radiation source analysis of beamline stations at fourth-generation synchrotron light facility. *Radiation Measurements* 189:107528

[10] Zhou Z, Du X, Yang J, Wang Y, Li C, et al. 2016. The vacuum ultraviolet beamline/endstations at NSRL dedicated to combustion research. *Journal of Synchrotron Radiation* 23(4):1035−1045

[11] Xu Q, Liu B, Chen W, Yu T, Zhang Z, et al. 2022. Comprehensive study of the low-temperature oxidation chemistry by synchrotron photoionization mass spectrometry and gas chromatography. *Combustion and Flame* 236:111797

[12] Fófano JH, Ribas MH, Fujimoto MM. 2024. Photoionization cross sections of ethylene oxide. *Journal of Physics B: Atomic, Molecular and Optical Physics* 57(3):035201

[13] Yang JZ, Combustion Team. 2017. *Photoionization Cross Section Database (Version 2.0)*. Hefei: National Synchrotron Radiation Laboratory. http://flame.nsrl.ustc.edu.cn/database/ (accessed on 20 May 2024)

[14] Frisch MJ, Trucks GW, Schlegel HB, Scuseria GE, Robb MA, et al. 2019. Gaussian 16, Revision C.01. Wallingford, CT: Gaussian Inc. https://gaussian.com/gaussian16/ (accessed on 20 September 2023)

[15] Hehre WJ, Ditchfield R, Pople JA. 1972. Self—consistent molecular orbital methods. XII. Further extensions of Gaussian—type basis sets for use in molecular orbital studies of organic molecules. *The Journal of Chemical Physics* 56(5):2257−2261

[16] Krishnan R, Binkley JS, Seeger R, Pople JA. 1980. Self-consistent molecular orbital methods. XX. A basis set for correlated wave functions. *The Journal of Chemical Physics* 72(1):650−654

[17] Becke AD. 1993. Density-functional thermochemistry. III. The role of exact exchange. *The Journal of Chemical Physics* 98(7):5648−5652

[18] Fukui K. 1981. The path of chemical reactions—the IRC approach. *Accounts of Chemical Research* 14(12):363−368

[19] Raghavachari K, Trucks GW, Pople JA, Head-Gordon M. 1989. A fifth-order perturbation comparison of electron correlation theories. *Chemical Physics Letters* 157(6):479−483

[20] Dunning TH, Jr. 1989. Gaussian basis sets for use in correlated molecular calculations. I. The atoms boron through neon and hydrogen. *The Journal of Chemical Physics* 90(2):1007−1023

[21] Georgievskii Y, Miller JA, Burke MP, Klippenstein SJ. 2013. Reformulation and solution of the master equation for multiple-well chemical reactions. *The Journal of Physical Chemistry A* 117(46):12146−12154

[22] Eckart C. 1930. The penetration of a potential barrier by electrons. *Physical Review Journals Archive* 35(11):1303−1309

[23] Wang X, Ye L, Zhang X, Zhang Z, Yang J, et al. 2023. Reaction kinetics and implications of the decomposition and formation of C_2H_4O isomers. *Combustion and Flame* 250:112634

[24] Reaction Mechanism Generator (RMG). Molecule Search. Cambridge: Massachusetts Institute of Technology. https://rmg.mit.edu/molecule_search (accessed 16 Aug 2023)

[25] Zhou CW, Li Y, Burke U, Banyon C, Somers KP, et al. 2018. An experimental and chemical kinetic modeling study of 1,3-butadiene combustion: ignition delay time and laminar flame speed measurements. *Combustion and Flame* 197:423−438

[26] Fu W, Li Y, Liang C. 2019. Dehydrogenation mechanism of ethanol on Co(111) surface: a first-principles study. *Acta Chimica Sinica* 77(6):559−568